Hydrometeor Detection Using *Cloudsat*—An Earth-Orbiting 94-GHz Cloud Radar

ROGER MARCHAND

Joint Institute for the Study of the Atmosphere and Ocean, University of Washington, Seattle, Washington

GERALD G. MACE

Department of Meteorology, University of Utah, Salt Lake City, Utah

THOMAS ACKERMAN

Joint Institute for the Study of the Atmosphere and Ocean, University of Washington, Seattle, Washington

GRAEME STEPHENS

Department of Atmospheric Sciences, Colorado State University, Fort Collins, Colorado

(Manuscript received 16 March 2007, in final form 26 August 2007)

ABSTRACT

In late April 2006, NASA launched *Cloudsat*, an earth-observing satellite that uses a near-nadir-pointing millimeter-wavelength radar to probe the vertical structure of clouds and precipitation. The first step in using *Cloudsat* measurements is to distinguish clouds and other hydrometeors from radar noise. In this article the operational *Cloudsat* hydrometeor detection algorithm is described, difficulties due to surface clutter are discussed, and several examples from the early mission are shown. A preliminary comparison of the *Cloudsat* hydrometeor detection algorithm with lidar-based results from the *Cloud-Aerosol Lidar and Infrared Pathfinder Satellite Observation* (*CALIPSO*) satellite is also provided.

1. Introduction

Clouds play a major role in earth energy and water cycles. They cool the earth by reflecting sunlight back to space and warm the earth by absorbing and reemitting thermal radiation. By modulating the distribution of heating within the atmosphere and at the surface, clouds fundamentally influence the circulation of the atmosphere and oceans (Stephens et al. 2002). Much of our current knowledge of global cloud properties comes from the study of satellite-based visible and infrared passive imager data, collected over the past several decades. This imager perspective is now being enhanced with data from satellite-based radar and lidar systems that provide range-resolved data on the vertical structure of clouds and aerosols.

In late April 2006, the National Aeronautics and Space Administration (NASA) launched the *Cloudsat* and *Cloud-Aerosol Lidar and Infrared Pathfinder Satellite Observation* (*CALIPSO*) satellites. *Cloudsat* uses a near-nadir-pointing millimeter-wavelength radar to probe the vertical structure of clouds and precipitation, while *CALIPSO* combines an active lidar instrument with passive infrared and visible imagers to probe the vertical structure and properties of thin clouds and aerosols. *CALIPSO* and *Cloudsat* are separate satellites that fly in formation with three other satellites [*Aqua*, *Aura*, and *PARASOL* (*Polarization and Anisotropy of Reflectances for Atmospheric Sciences coupled with Observations from a Lidar*)]. Together, these satellites are part of a constellation of earth-observing satellites known as the A-Train. Thus, the *Cloudsat* observations, while of great interest by themselves, are also part of a larger observational strategy to understand the earth climate system (Stephens et al. 2002).

The first step in using *Cloudsat* observations is to distinguish clouds and other hydrometeors from radar noise. The *Cloudsat* project routinely generates a "cloud mask" (described in section 2) that indicates which radar observations are likely hydrometeors and provides a rough estimate of the likelihood that a given

Corresponding author address: Roger Marchand, Pacific Northwest National Laboratory, 902 Battelle Blvd., Richland, WA 99352.
E-mail: rojmarch@u.washington.edu

DOI: 10.1175/2007JTECHA1006.1

TABLE 1. Description of *Cloudsat* cloud mask values, false detection rates, and percentage of false detections. The percent of false detection is given by 100 times the number of false detections divided by the total number of detections for the specified cloud mask value.

Mask value	Meaning	% false detections goal	Estimated % false detection via *CALIPSO* comparison
−9	Bad or missing radar data		
5	Significant return power but likely surface clutter		
6–10	Very weak echo (detected using along-track averaging)	<50%	44%
20	Weak echo (detection may be artifact of spatial correlation)	<16%	5%
30	Good echo	<2%	4.3%
40	Strong echo	<0.2%	0.6%

detection is false. Here we describe the *Cloudsat* hydrometeor detection algorithm, discuss difficulties due to surface clutter, and show several examples from the early mission. We also provide a preliminary comparison of the *Cloudsat* hydrometeor detection algorithm with lidar-based results from *CALIPSO*.

The *Cloudsat* radar does not scan but generates a curtain, or two-dimensional cross section, through the atmosphere as the satellite moves along its orbital trajectory. In this article we refer to each element in this two-dimensional cross section as a range bin. The radar transmits pulses with an approximate duration of 3.3 μs and thus measures cloud and precipitation reflectivity with an effective vertical range resolution of approximately 480 m. The measured return power, however, is sampled at a rate equivalent to about 240 m in range; that is, the measured data are two times oversampled. Pulses are averaged about 0.16 s along the nadir track, yielding an effective footprint (6 dB) at the surface of about 1.4 km $\times$ 1.7 km for each radar profile. The minimum detectable signal from the *Cloudsat* radar is still under evaluation, but early results show that it is slightly exceeding expectations with a sensitivity of about −30 dBZ.[1]

2. Cloud mask and detection algorithm

a. Description of 2B-GeoProf product

The purpose of the *Cloudsat* hydrometeor detection algorithm is to identify when the measured radar return power is likely to be due to scattering by clouds or other hydrometeors and when it is likely to contain only noise. The result of the operational algorithm is a "cloud mask" that is stored in the *Cloudsat* operational Geometric Profile (2B-GeoProf) data product. The cloud mask contains a value between 0 and 40 for each range bin, with values greater than 5 indicating the location of likely hydrometeors. Increasing values indicate a reduced probability of a false detection, as summarized in Table 1. In addition to the cloud mask, this product contains the radar reflectivity (i.e., the calibrated measured return power), an estimate of gas absorption due to oxygen and water vapor on the observed reflectivity, and several quality indicator flags. Unlike typical weather radars, which operate at much longer wavelengths and are primarily designed to detect rain rather than clouds, the effect of water vapor on *Cloudsat* observed reflectivity can be significant. Two-way attenuation from the surface to the satellite of more than 5 dBZ is not unusual in the tropics. No estimate of loss in reflectivity due to absorption or scattering by hydrometeors is included in GeoProf, and users are cautioned that losses of 10 dB km^{-1} or higher are possible with large liquid water contents. At times, the *Cloudsat* radar is fully attenuated, or attenuated to the point where multiple scattering dominates the measured return power (Mace et al. 2007).

The cloud mask, reflectivity field, and gaseous absorption are all provided on a height grid with 125 vertical range bins, where the *Cloudsat* range bin closest to mean sea level has been placed in vertical bin 105. The location of the range bin that is closest to the actual surface location is also provided.

b. Description of the hydrometeor detection algorithm

The *Cloudsat* hydrometeor detection algorithm is similar to the algorithm developed by Clothiaux et al. (1995, 2000) but with two significant changes: 1) a power probability weighting scheme and 2) an along-track integration scheme. The along-track integration

[1] The sensitivity (sometimes also referred to as the minimum detectable signal) is defined as the point where the radar noise power equals the target power. Because the scattered power from distributed hydrometeors decreases as the distance from the radar squared and the noise power is reduced by the square root of the averaging time, the sensitivity is a function of the distance from the radar and the averaging time. As such, any expression of radar sensitivity should be accompanied by a reference range and averaging interval. *Cloudsat* flies more than 700 km above the earth surface (which can be taken as the reference range). Because of this large distance, the change in sensitivity over the troposphere is negligible.

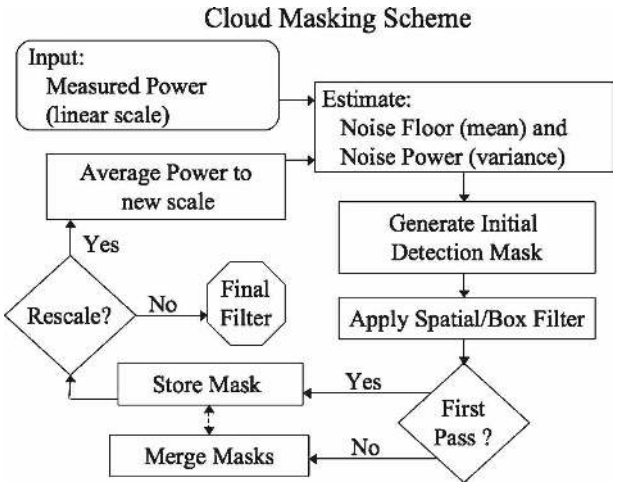

FIG. 1. Cloud masking scheme.

scheme helps identify targets that are too weak to be detected at full resolution (0.16 s) but can be detected through along-track (temporal) averaging of the data.

A schematic of the detection algorithm is given in Fig. 1. The input to the routine is the raw radar measured return power (P_{raw}), provided in the level 1B Cloud Profiling Radar (CPR) data product. An estimate of the mean and variance of the radar-measured noise power is determined using the measured return power from the stratosphere where the presence of any hydrometeor—such as polar stratospheric clouds—would have a volume-integrated backscatter cross section much less than the detection threshold of the radar. Therefore, any power in these range bins is due primarily to microwave emission by the radar components, but also contains contributions from microwave emission by the earth surface and gases such as water vapor in the atmospheric column. The mean noise power (P_n) and its standard deviation (σ_{P_n}) at each along-track sample are calculated using a moving-average filter that is 10 range bins in the vertical and 2 along-track bins wide.

An initial set of hydrometeor detections is determined by comparing the target power ($P_T = P_{\text{raw}} - P_n$) with σ_{P_n}. Any range bin where $P_T > \sigma_{P_n}$ potentially contains backscattered power due to hydrometers. However, because of random fluctuations in the noise (which is Gaussian distributed), there is about a 16% chance that any range bin will have $P_T > \sigma_{P_n}$ due solely to noise, that is, a potential false detection.

The detection algorithm starts by creating an initial cloud mask (with the same dimensions as the input return power matrix) with values ranging from 0 to 40. For range bins where $\sigma_{P_n} < P_T < 2\sigma_{P_n}$, the cloud mask is set to a value of 20; if $2\sigma_{P_n} \le P_T < 3\sigma_{P_n}$, the mask is set to 30; if $P_T \ge 3\sigma_{P_n}$ the mask is set to 40; otherwise it is set to 0. We reserve values of 10 or less in the cloud mask to indicate clutter or the detection of clouds with signal power P_T less than σ_{P_n}, which we discuss momentarily.

To reduce the occurrence of false detections (which are uniformly randomly distributed) and to reliably identify range bins with hydrometeors whose P_T is not much different from P_n, a spatial box filter is applied. Following Clothiaux et al. (1995), a box is centered over each range bin of a size N_w (range bins along track) by N_h (range bins in the vertical). We then count the number (N_0) of range bins in the box where $P_T > \sigma_{P_n}$, not counting the center range bin. If P_n is Gaussian distributed and independent in each range bin, the probability (p) of any particular configuration with N_0 of the total ($N_T = N_w N_h - 1$) range bins would have a $P_T > \sigma_{P_n}$ solely because random noise is less than or equal to

$$p \le G(L)(0.16^{N_0})(0.84^{N_T - N_0}), \tag{1}$$

where G is the probability that the center pixel could be a false detection for a cloud mask value of level L [$G(0) = 0.84$, $G(20) = 0.16$, $G(30) = 0.028$, $G(40) = 0.002$].

We expect that hydrometeor occurrence is highly spatially correlated over spatial scales of N_w by N_h range bins, and it is likely that, if a cloud is present, many range bins in the box will contain significant backscatter power (i.e., $P_T > \sigma_{P_n}$). Thus, if p given by Eq. (1) is found to be less than some threshold value (i.e., $p < p_{\text{thresh}}$), then the center range bin is unlikely to be noise and a hydrometeor (or other target) is likely present. In this situation, the cloud mask for the center range bin is then set to a value of 20 if it was 0 in the initial cloud mask; otherwise the value in the initial cloud mask is retained. Likewise, if $p > p_{\text{thresh}}$, then the measured power could well be noise and the cloud mask is set to 0, regardless of the initial cloud mask value. Following Clothiaux et al. (1995) this box filter is applied to the data several times in succession. In each pass of the box filter some nominally false detections are removed, and the effect of removing these detections is propagated to nearby pixels in the next pass. After a few passes one begins to remove more cloud (i.e., generate more failed detections) than to remove true false detections. Like Clothiaux et al. we found two or three passes appeared nominal.

The algorithm described up to this point is identical to that given by Clothiaux et al. (1995) except for the (center pixel) power weight in Eq. (1), that is, the factor G. We will discuss the purpose of the power weight in section 2c.

Having visually examined data from eight aircraft flights and months worth of ground-based radar data

(both modified to look like less-sensitive *Cloudsat* measurements, including the oversampling), as well as early-mission *Cloudsat* observations, we have found that

$$p_{\text{thresh}} = (0.16^{N_{\text{thresh}}})(0.84^{N_T - N_{\text{thresh}}}), \qquad (2)$$

with $N_w = 7$, $N_h = 5$, $N_{\text{thresh}} = 20$ (or equivalently $p_{\text{thresh}} \sim 10^{-17}$) and three passes of the box filter produces good results, by which we mean that the algorithm is stable and appeared to produce few failed detections and a low rate of false detections. These filter parameters will be periodically evaluated throughout the *Cloudsat* mission, but are not expected to change.

For the algorithm to be stable, N_{thresh} must be chosen larger than $\frac{1}{2} \times (N_h - 1) \times N_w$ or 14 in our configuration. To understand this, imagine that we have a perfectly flat strongly reflecting cloud many kilometers wide and examine a range bin directly above the cloud layer. In this case, the bottom rows of the box filter will all have significant power so we will have a value for N_0 of at least $\frac{1}{2} \times (N_h - 1) \times N_w$. Therefore, if we do not choose N_{thresh} larger than this value, we will always mark any range bin above the cloud layer ON (a positive detection), even if the range bin contains no cloud. Further, when we apply the filter repeatedly the cloud will artificially expand. In application we also do not want a few false positives above the cloud boundary to falsely activate a clear range bin. Choosing $N_{\text{thresh}} = 20$ means 6 additional range bins must have significant power (which will happen by chance only about 10% of the time for our configuration with 21 bins above the cloud boundary). We could choose N_{thresh} to be larger than 20 to reduce the false detections, but we also do not want to fail to detect true cloud-filled range bins. For example, imagine a perfectly square cloud and examine the bin containing the corner of the cloud. The corner has $N_o = \frac{1}{4} \times (N_h + 1) \times (N_w + 1) = 15$. As a result, the algorithm will tend to indicate corners of true clouds are likely false detections. The tendency to remove corners is partially corrected by the power-weighting scheme in the case of clouds with high signal to noise (as will be shown in section 2c). Nonetheless one wants to set N_{thresh} low to minimize failed detections.

To improve the detection capability, the *Cloudsat* algorithm is designed to average the raw return power in the along-track direction. The purpose of this portion of the algorithm is to find condensate that is horizontally extensive (well beyond the size of the single radar profile) but below the single-profile sensitivity limit of the radar. We used four levels of along-track averaging with 3-, 5-, 7-, and 9-bin-wide averaging windows. At each level, a separate cloud mask is created and merged in sequence, starting with the cloud mask created without any along-track averaging. That is, we create a new cloud mask based on 3-bin along-track averaging and then merge this 3-bin-cloud mask with a cloud mask created without any along-track averaging (what one might call a 0-bin cloud mask). We then create a cloud mask based on 5-bin along-track averaging and merge this 5-bin cloud mask with the already combined 3-bin + 0-bin mask etc.

By applying a moving average to the data, the noise and target power become increasingly spatially correlated, thereby violating the independence assumption used in the spatial filter, Eq. (1). By trial and error, we found that using along-track averages of 3, 5, 7, and 9 bins for *Cloudsat* required increasing N_{thresh} (to compensate for the additional correlation) to values of 23, 25, 27, and 29, respectively. In addition to increasing $N_{\text{thresh,}}$ we also only allow range bins to be marked as containing a likely hydrometeor in the moving-averaged cloud masks if they initially contain a significant return (i.e., $P_T > \sigma_{P_n}$). Thus, unlike the cloud mask created without along-track averaging, no range bin in the 3-bin-average mask can have a value greater than zero simply because it is surrounded by other likely detections.

To merge each new moving-average mask with a previous mask, the new mask is compared with a reduced-resolution version of the previous mask. This reduced-resolution previous mask is constructed by taking a moving average of the previous mask. The merged or combined mask is then given by the previous mask plus those range bins found to have both (i) values greater than zero in the new mask and (ii) values of zero in the reduced-resolution version of the previous mask. This last step prevents objects identified in the previous mask from being artificially expanded by the moving-average process. The new detections are given a cloud mask value of 11 minus the mask level number (which varies from 1 up to 4). Thus, cloud mask values of 6 to 10 indicate weak targets and specify the number of along-track bins averaged. Finally, after all levels are complete, the cloud mask is run through the spatial box filter a final time. This last filtering does allow pixels to be turned ON because of position (e.g., if a seemingly cloud-free pixel is completely surrounded by likely detections).

c. Simple test results

Figure 2 shows the results of applying the hydrometeor detection algorithm of section 2b to a simple test pattern. The test pattern, shown in Fig. 2a, consists of a Gaussian noise background (with uncorrelated noise in each range bin), a sequence of seven square targets (with sides ranging from 100 bins to only 3 bins long),

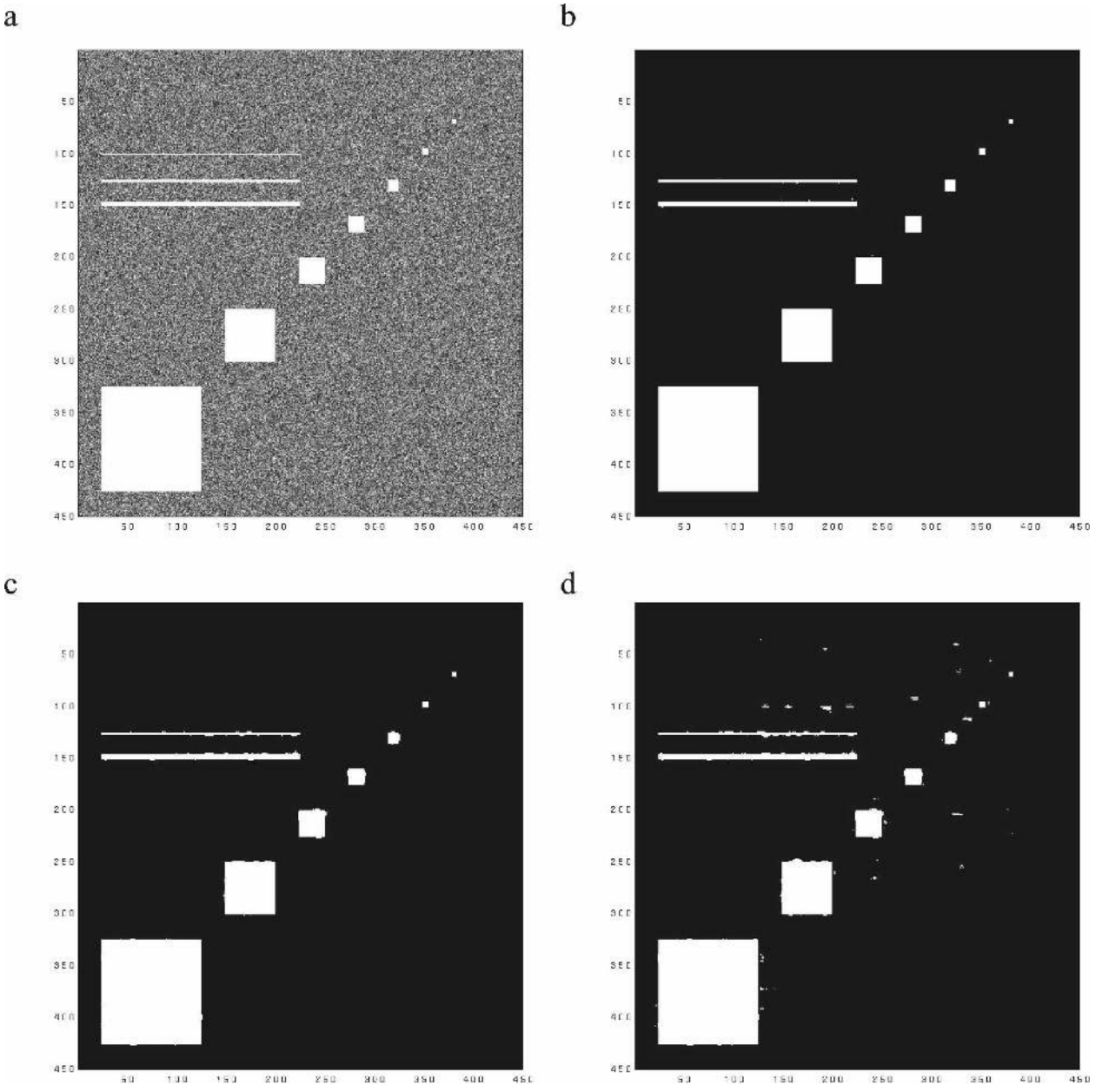

FIG. 2. *Cloudsat* algorithm applied to test pattern, with test object target signal equal to 10 sigma: (a) input to detection algorithm, (b) cloud mask confidence level greater than 30, (c) cloud mask confidence level greater than 20, and (d) cloud mask confidence level greater than 0.

and three line targets with widths of 1, 2, and 4 bins. In this first test, the targets are strong with a signal level set to 10 times σ_{P_n}. This is a strong signal, such that if we were constructing a cloud mask based on simple threshold of the observed signal in each bin, we would be 99.99% confident that these bins contained a cloud. Figure 2b shows the cloud mask where values of 40 are shown in white and those with values less than 40 in black. Values of 40 indicate a strong detection (at least 3 times σ_{P_n}). Figure 2b also shows that the hydrometeor detection algorithm does an excellent job, detecting all seven of the square targets and two of the three line targets with almost no false detections (at level 40). The algorithm does not find the line target that is only one pixel wide, even though the signal is strong, because the spatial filter requires a greater level of spatial correlation than is present for the one-pixel-wide line. *Cloudsat* measurements are 2 times oversampled in the ver-

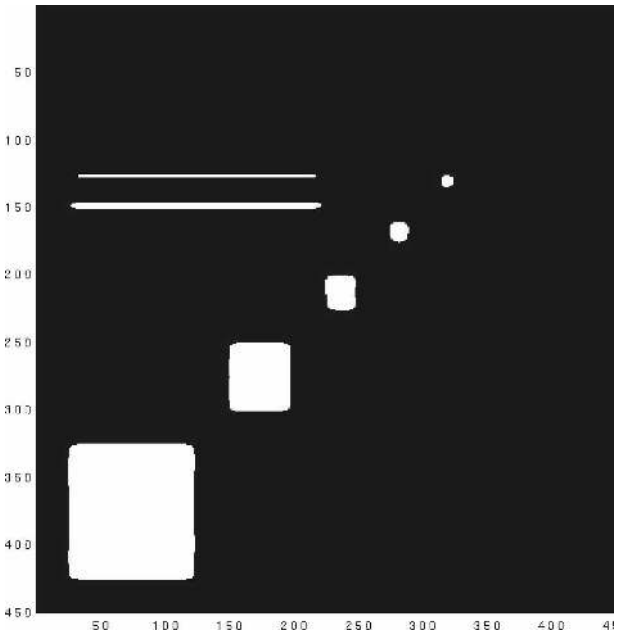

FIG. 3. As in Fig. 2b, but without center-pixel power-weighting scheme.

tical, so all strong signals will occupy at least two vertical range bins.

Figure 2c shows the cloud mask with values of 20 or more given in white and Fig. 2d shows the cloud mask with all detections, including those found with along-track averaging. Not surprisingly, we observe an increase in the number of false detections at these lower confidence levels. In both cases, noise near the true targets tends to pass through the spatial filtering. The along-track averaging scheme (cloud mask values between 6 and 10), in particular, is designed to be aggressive in finding possible targets, and so also tends to identify clusters of higher-than-average noise.

Earlier we mentioned that the *Cloudsat* scheme is similar to the algorithm of Clothiaux et al. (1995) except that Clothiaux et al. considered all detections as binary (either yes or no), while our Eq. (1) takes into account strength of the measured power. The power weighting makes it more difficult to remove range bins with large signal-to-noise ratios from the cloud mask. This reduces the tendency of the Clothiaux et al. algorithm to round off the edges of clouds. The rounding occurs because there is an insufficient number of cloud-filled bins near the corner of objects to prevent the spatial filter from removing the edges. Figure 3 shows the results of applying the hydrometeor detection algorithm without the power weighting to the same test data shown in Fig. 2a. A similar effect is demonstrated in Fig. 6 of Clothiaux et al. (1995). Comparing Fig. 3 with Fig. 2b shows that only five of the seven test squares are identified. The 3×3 and 5×5 squares are lost entirely, while the other squares are rounded. The 2- and 4-pixel-wide line targets are detected, but the ends of the lines are also rounded.

Figure 4 summarizes the performance of the hydrometeor detection algorithm for this simple test, providing the number of false detections (range bins where there is no actual target, but the hydrometeor detection algorithm indicated there likely is a target) and the number of failed detections (range bins where there is a target, but the detection algorithm indicated none was likely). The false detections and failed detections (sometime referred to as false negatives), are shown as a function of the cloud mask confidence values. Without the power weighting, more than 7% of the target bins are not detected; however, on the positive side, there are essentially no false detections. With the power-weighting scheme, only a small percentage of targets are missed, and almost all of these missing pixels are the line target that was only one range bin wide. The false detections with the power-weighting scheme are nearly zero at confidence level 40, and even with the along-track averaging remain less than 0.5% (by volume).

It should be pointed out that Clothiaux et al. (1995) wanted only a simple yes/no cloud mask and, for their application, a minimum of false detections. They were less concerned with missing detections and specifically noted the conservative nature of the cloud mask they

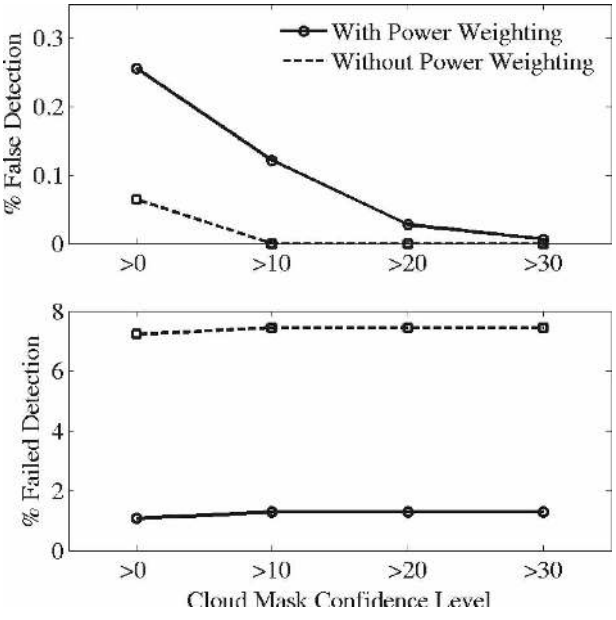

FIG. 4. Summary of failed detections (places where cloud mask indicates clear where there is signal) and false detections (places where cloud mask indicates clouds, but where only radar noise is present).

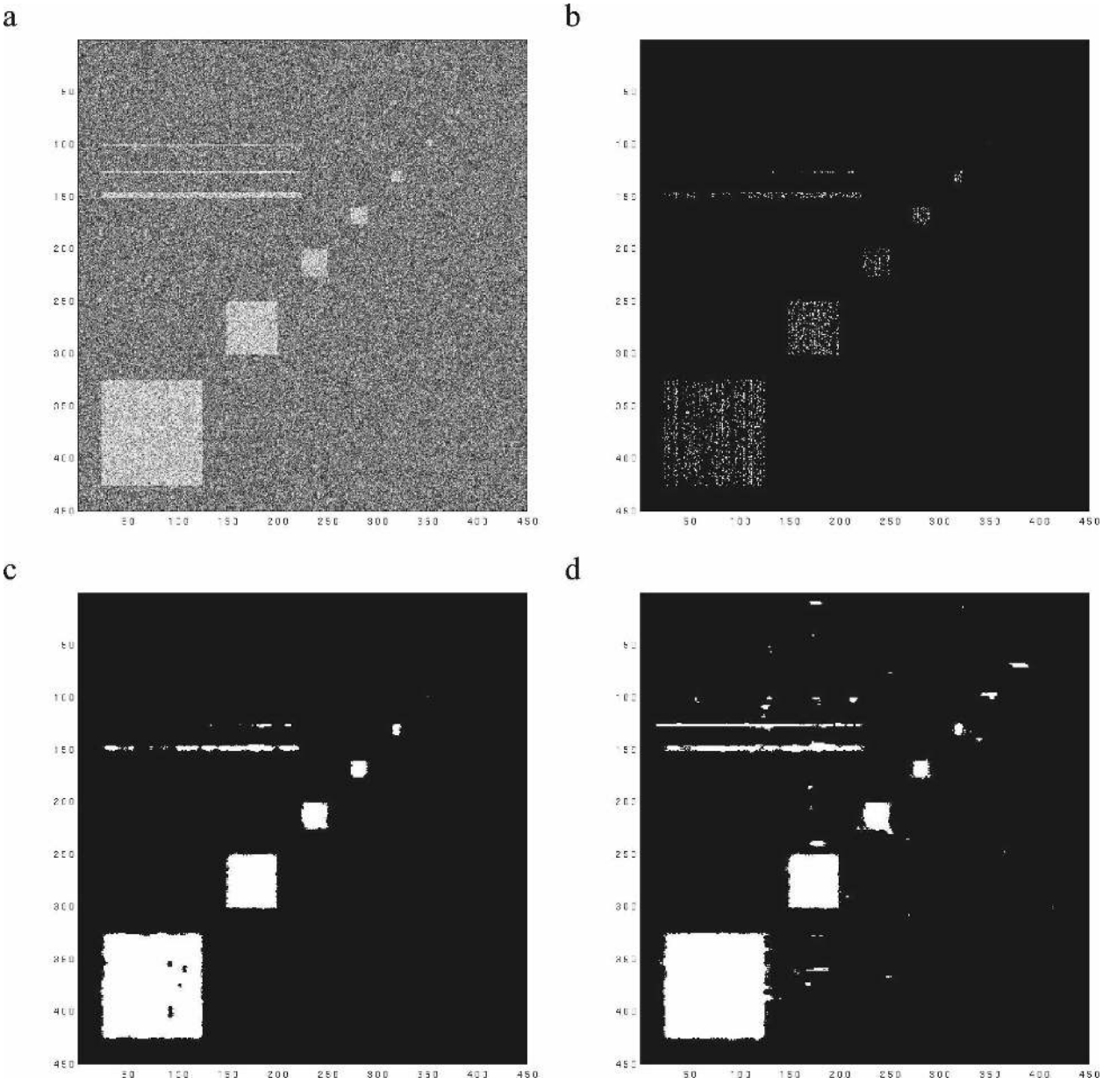

FIG. 5. As in Fig. 2, but with test object mean signal equal to 2 sigma.

created, which they estimated could be missing as much as 15% of detectable hydrometeors.

Figures 5 and 6 demonstrate the performance of the *Cloudsat* scheme for the same simple target set used in Fig. 2, but the target power ($P_T = P_{\text{raw}} - P_n$) has been reduced to 2 times and 0.5 times the standard deviation in the noise power (σ_{P_n}), respectively. This is equivalent to a target power ($P_T = P_{\text{raw}} - P_n$) that is 3 dB above and 3 dB below σ_{P_n}.

In Fig. 5, we see that random noise fluctuations increase the total measured power such that some of the target bins are identified with high confidence (mask level = 40), even though none of the target bins actually have a strong signal. At mask level 20, five of the seven target squares and most line targets are found. Using the along-track averaging (mask level >5) all seven targets are found, although their size is exaggerated because the along-track averaging effectively reduces the resolution of the measured power and cloud mask.

The targets as shown in Fig. 6 are extremely weak. The hydrometeor detection algorithm can only find the targets using the along-track averaging. As shown in

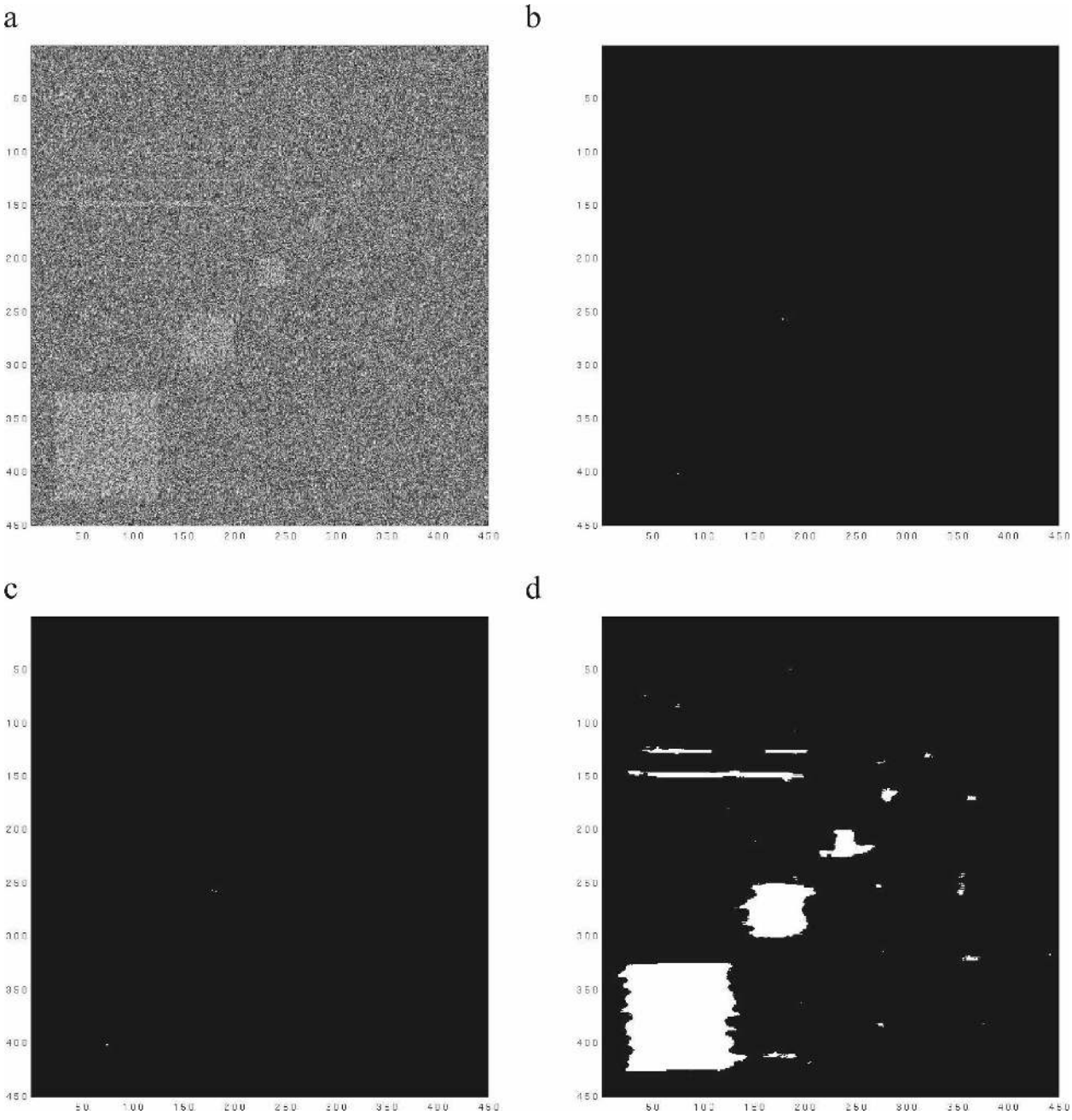

FIG. 6. As in Fig. 2, but with test object mean signal equal to 0.5 sigma.

Fig. 6d, the mask is able to identify the presence of five of the seven target squares and much of the line targets (Fig. 6d). There is not enough power in the along-track direction (horizontal) to make the small squares detectable because they are not sufficiently extensive targets. After running this test many times (thereby varying the pattern of the background noise), the percentage of missed detections was found to vary from 9% to 15% and the false detections varied from 0.6% to 1.2% (by volume).

Note that the along-track algorithm does not maintain the sharp boundaries of the target squares. In part, this is because the along-track scheme only averages in the along-track direction. Given the 480-m vertical resolution of *Cloudsat*, averaging in the vertical does not yield much benefit and makes spatial filtering problematic. However, the algorithm described here could be modified to take advantage of vertical averaging for radars with higher vertical resolution or greater oversampling rates.

d. Surface clutter

The nature of the *Cloudsat* measurements near the surface is an important issue. The outgoing radar pulse is not a perfect square wave, but has a finite rise time. Because the surface is typically two to five orders of magnitude more reflective than hydrometeors, interaction between the surface and the edge of the radar pulse (which extends outside the nominal 480-m resolution volume) can contribute significant signal relative to that of potential near-surface hydrometeors. Figure 7 shows an estimate of the clear-sky observed return power for a typical orbit.[2] Measurements in the range bin closest to the surface and, because of oversampling, the bin directly above this bin, are expected to be dominated by the surface return. Figure 7 demonstrates that the surface clutter unfortunately extends into the second, third, and fourth bins above the surface. It is only for the fifth range bin (~1.2 km) above the surface that the signal returns approximately to the nominal sensitivity.

As a result of the surface contamination, all cloud mask detections below roughly the 99th percentile of the clear-sky return (dashed lines in Fig. 7) are currently being set to a value of 5, to indicate there is return power above the radar noise floor but the signal is indistinguishable from surface clutter. While this conservative threshold should keep the false detection rate (by volume) below 1%, it also means that typically only rain and heavy drizzle can be detected in the third bin above the surface (~720 m) and moderate drizzle in the fourth bin (~860 m). The percentage of false detections will also be larger between the surface and about 2 km, than above 2 km. Initial estimates suggest the false detection rate is about twice as high below 2 km as above it. (Note the values derived in section 3 and given in Table 1 include all altitudes.)

Subtracting an estimate of the surface clutter from the total measured return power in the second through fourth range bins above the surface is currently being investigated and will be included in the next version of the data product (R04). Preliminary assessment of such a clutter rejection algorithm shows reductions in clutter of 10–20 dB over ocean surfaces.

3. Examples from *Cloudsat* and *CALIPSO*

Figures 8, 9, and 10 show examples of *Cloudsat* observed reflectivity along with the cloud mask obtained using the procedure described in section 2. Each example consists of 1000 profiles. The first example, Fig. 8, consists primarily of a high, thin cirrus cloud that increases in thickness from left to right. In the *Cloudsat* cloud mask (Fig. 8b), the detections that result from the along-track integration scheme (values of 10 or less) are represented by the light blue (cyan) color. The full extent of this cirrus layer is more readily apparent from *CALIPSO* lidar observations. Figures 8c and 8d show the *CALIPSO* lidar 532-nm total backscattering and derived vertical feature mask (VFM; Vaughan et al. 2004). *CALIPSO* is a separate satellite from *Cloudsat*, but flies along nearly the same orbit path, about 20 s behind *Cloudsat*. The *CALIPSO* data in Fig. 8 are plotted for the same latitude and longitude range as shown for *Cloudsat*. The *CALIPSO* 532-nm lidar data show a sharply defined cirrus cloud as well as scattering in the boundary layer by a mixture of cloud and aerosols. The *CALIPSO* data shown here are the first publicly released data (Prov-V1–10) and are of only provisional quality.

The *CALIPSO* feature mask identifies where there is backscatter from cloud or aerosol particles and tries to differentiate between these feature types, as indicated in Table 2. Blue (value 2) indicates a cloud, cyan (value 3) indicates aerosol, and red (value 7) indicates areas where the lidar is totally attenuated. The identification of cloud in the boundary layer by the lidar is somewhat noisy, except near the middle of the image where there are distinctive water layers and the lidar is attenuated before reaching the surface. *Cloudsat*, at best, weakly detects some of the boundary layer cloud.

To compare the *Cloudsat* and *CALIPSO* cloud masks directly, on a range-bin-by-range-bin basis, we have mapped the *CALIPSO* feature mask onto the *Cloudsat* grid. The mapping is accomplished by first locating the nearest *CALIPSO* profile (in latitude and longitude) to each *Cloudsat* profile. Based on the latitude and longitude coordinates supplied by each satellite project, the nearest *CALIPSO* profile typically intersects the surface within about 1 km of the *Cloudsat* profile. Despite this level of collocation (1 km in space and 20 s in time), there are places (though not in this example) where offsets are clearly apparent. Because *CALIPSO* vertical resolution is higher than *Cloudsat*, we next locate the set of *CALIPSO* range bins within

[2] At the beginning of the *Cloudsat* mission, the radar was unknowingly pointed 1.7° off nadir. This was corrected starting with orbit 1023, and the radar pointed directly toward nadir. However, it was found that pointing directly at nadir increased the surface reflectance and the effect of surface clutter approximately 10 dB due to specular reflection. Thus, starting with orbit 1595 (2000 UTC 15 Aug) the instrument was set to point 0.16° of nadir. This angle put the specular reflection in the first antenna null and reduced the surface clutter to previous levels. Data from these time periods are referred to as epic "E" 00, 01, and 02 (given in each file name), respectively. Data shown here are "typical" for data in epic 00 and the data now being collected in epic 02.

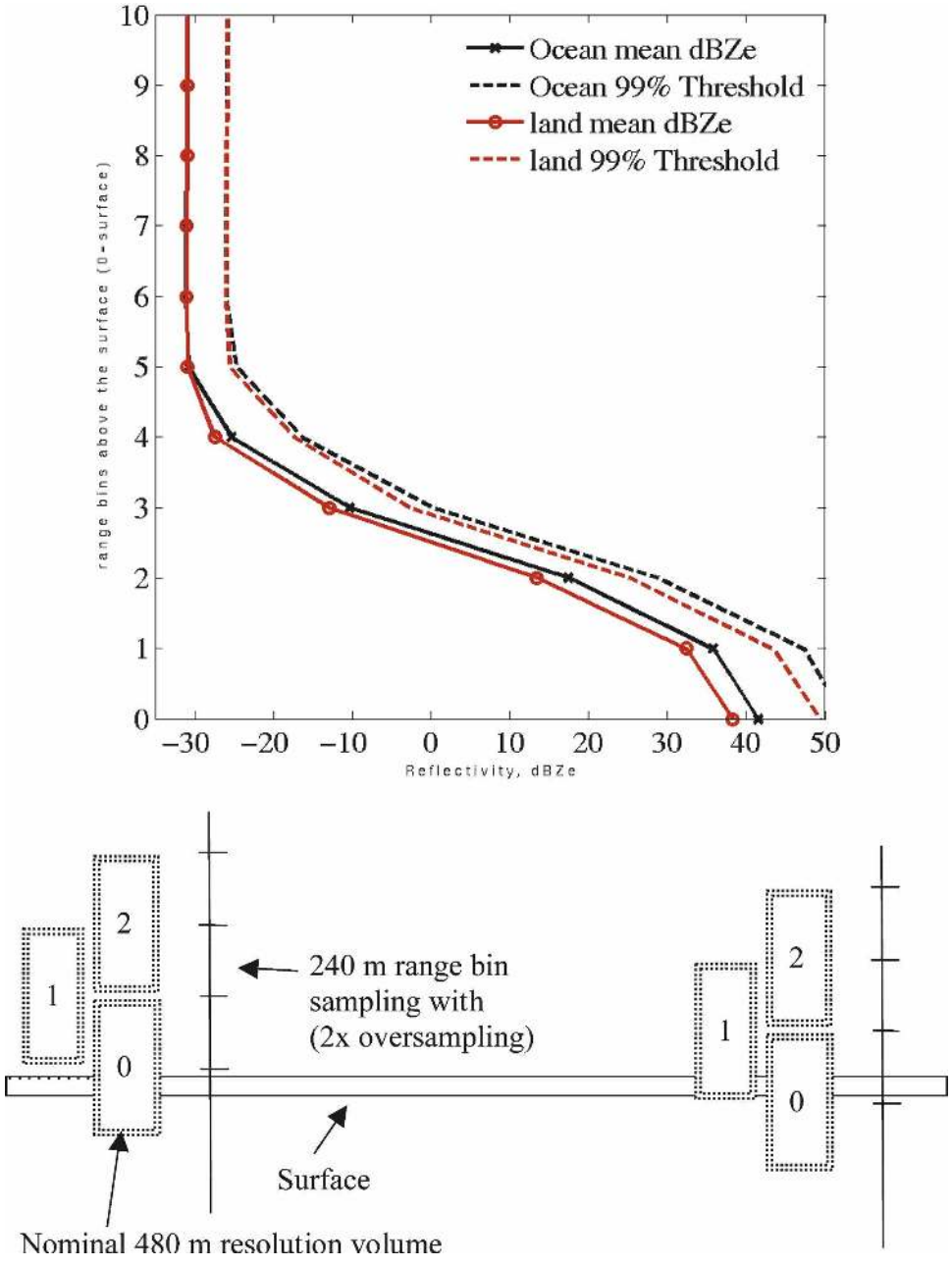

FIG. 7. (top) Typical (estimated) surface clutter profile (orbit 1596). (bottom) Bin 0 is defined as the range bin whose center is closest to the surface. Because of oversampling, bin 1 may or may not directly overlap the surface.

the 480-m *Cloudsat* resolution volume. The *CALIPSO* lidar gathers data at about 333-m horizontal and 30-m vertical resolution, but the data are averaged to 1-km horizontal and 60-m vertical between 8.2- and 20-km altitude. If any of the *CALIPSO* range bins in this set has a value of 2 in the associated vertical feature mask, we set the mapped-*CALIPSO* cloud mask to a value of 2 (meaning cloud present). Otherwise, we set the mapped-*CALIPSO* cloud mask to the largest value in the feature mask set.

To compare the masks directly, we then difference a binary version of the *Cloudsat* mask—where all range bins with a cloud mask value >5 are set to 1 and 0 otherwise—with a binary version of the *CALIPSO* cloud mask. In the binary *CALIPSO* cloud mask all range bins with a value of 2 or (where the binary *Cloud-*

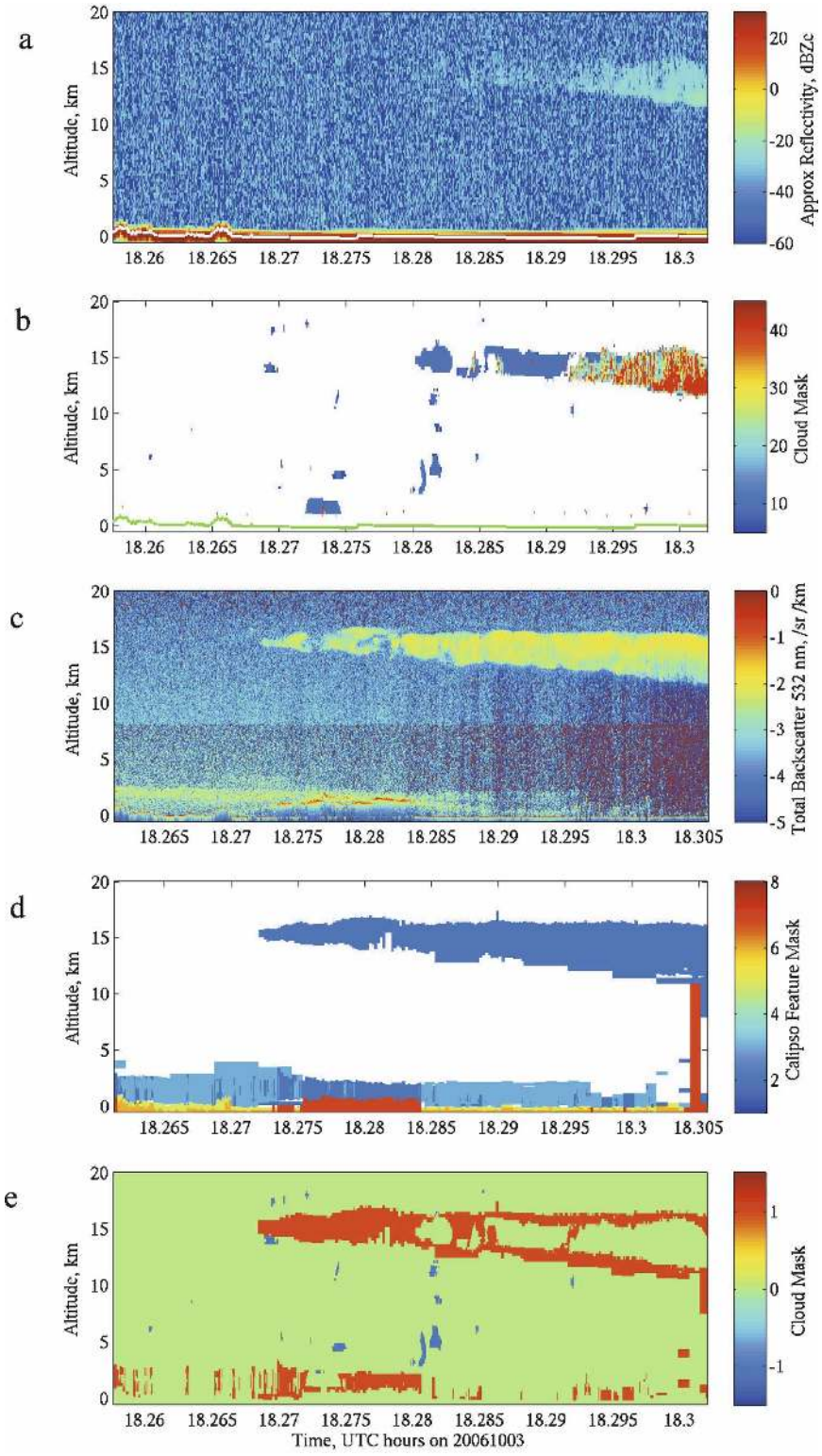

FIG. 8. Example of thin cirrus. (a) *Cloudsat* radar reflectivity, (b) *Cloudsat* cloud mask, (c) *CALIPSO* 532-nm total backscatter, (d) *CALIPSO* vertical feature mask, and (e) difference mask. In the difference mask, blue regions denote false detections: range bins where the *Cloudsat* mask suggests hydrometeors are likely present but there is no detection in the *CALIPSO* feature mask (cloud or aerosol) nor does the *CALIPSO* feature mask indicate the lidar is attenuated. Orange-red regions denote failed detections: range bins where the *CALIPSO* feature mask identifies clouds, but where *Cloudsat* does not detect hydrometeors.

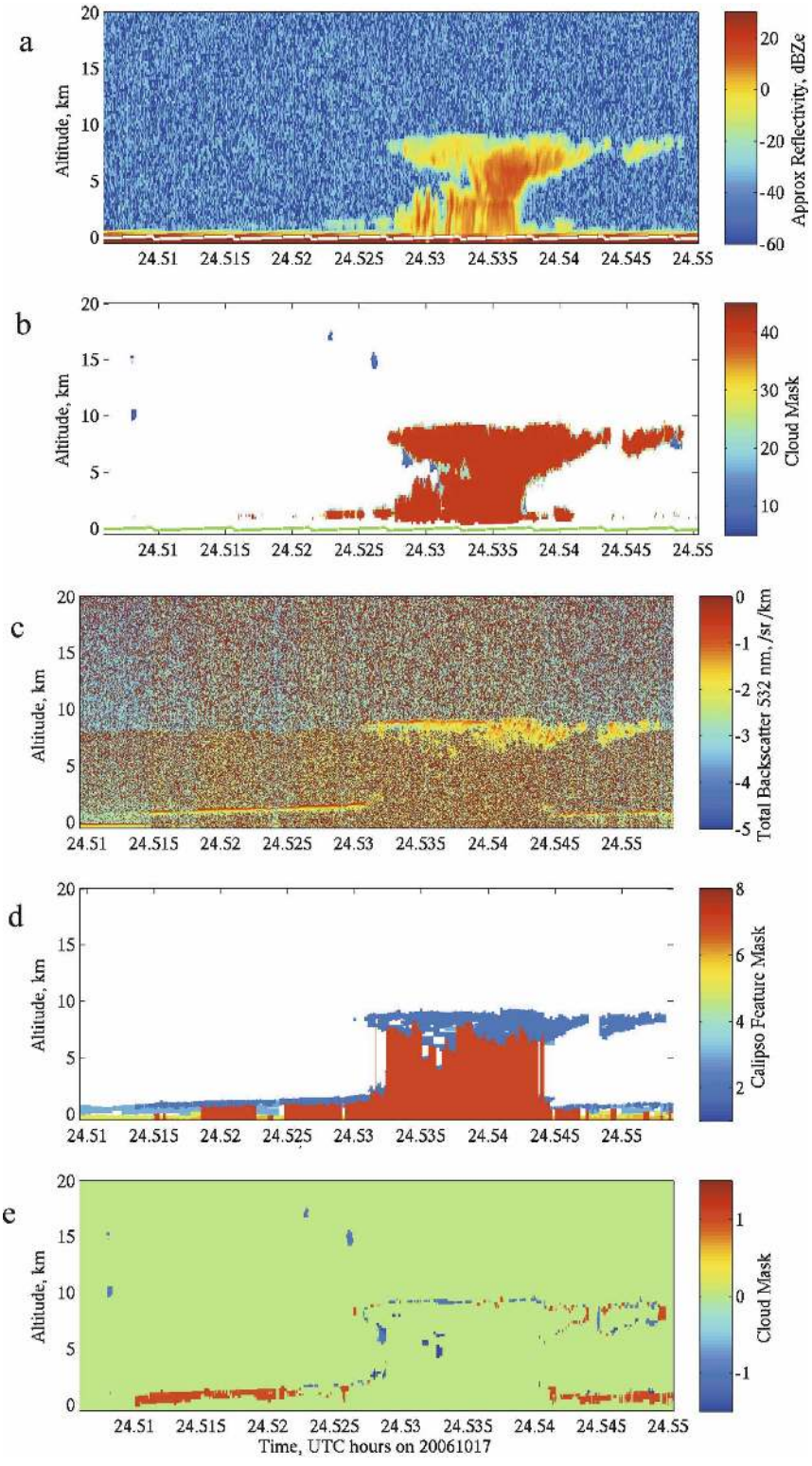

FIG. 9. Example of convection and boundary layer clouds. (a)–(e) As in Fig. 8.

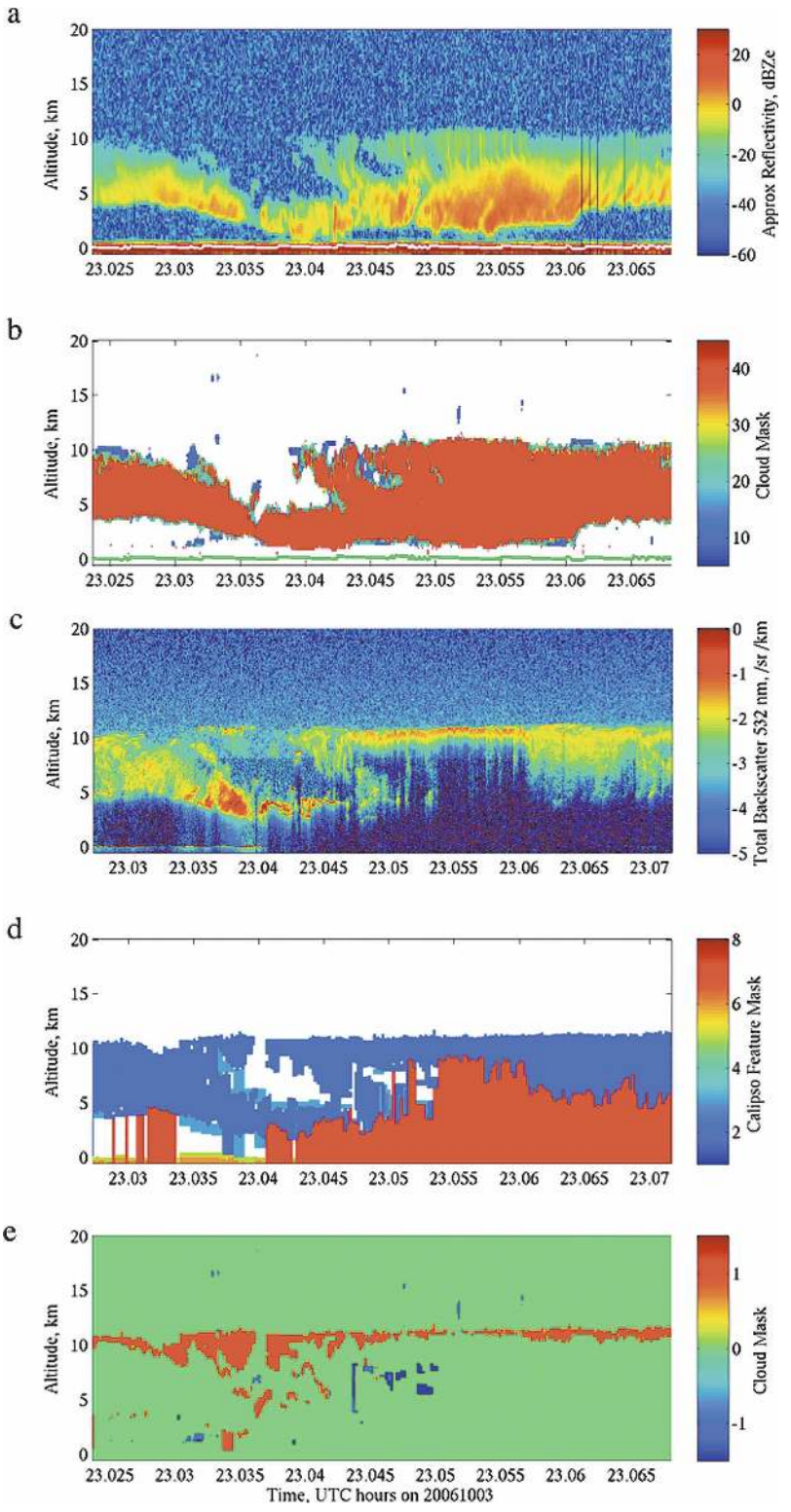

FIG. 10. Example of frontal cloud system. (a)–(e) As in Fig. 8.

TABLE 2. Description of *CALIPSO* vertical feature mask and feature types.

Value	Feature type
1	"Clear air"
2	Cloud
3	Aerosol
4	Stratospheric feature
5	Surface
6	Subsurface
7	No signal (totally attenuated)

sat mask is 1 and the *CALIPSO* mask has a value of 3 or 7) are set to 1 and 0 otherwise. The later condition (given in parentheses) on the *CALIPSO* mask prevents areas where the lidar is attenuated or has falsely identified aerosols rather than cloud from being considered cloud-free. The difference of the binary cloud masks (*CALIPSO* − *Cloudsat*) is shown in Fig. 8e. Range bins where *CALIPSO* detected a cloud but *Cloudsat* did not appear orange-red. The orange-red bins are failed detections by *Cloudsat*. Dark blue bins, on the other hand, represent false detections; that is, range bins where *Cloudsat* indicates the presence of hydrometeors is likely, but *CALIPSO* failed to detect them and most likely would have if they were present.

Given its sensitivity limit, it is not surprising that *Cloudsat* does not detect the entire cirrus layer. This limitation was understood from the genesis of the mission. Ultimately, retrievals of cloud particle size and condensate from *Cloudsat* and *CALIPSO* (in combination with other A-Train sensors) will be used to characterize the clouds that are detected by *Cloudsat* as well as those clouds that are only detected by *CALIPSO*.

This example was selected to highlight the strengths and weakness of the along-track integration scheme. While the along-track integration scheme effectively extends the sensitivity of the *Cloudsat* radar for horizontally extensive clouds, it also introduces a sizeable number of false detections. For this particular scene, approximately 20% of all the *Cloudsat* detections with a cloud mask value of 10 or less are false detections. We have analyzed 16 full orbits of data and found that, for any given orbit, 35%–65% of the *Cloudsat* detections due to the along-track integration scheme are false detections compared to the preliminary *CALIPSO* operational vertical feature mask. The mean value for all analyzed orbits is about 44%. The percentage of false detections for all the *Cloudsat* cloud mask confidence levels are shown in Table 1 (fourth column).

Figure 9 shows a similar set of panels as Fig. 8, but for a scene composed of developing convection and boundary layer clouds. The *CALIPSO* lidar (Fig. 9c,d) is only able to penetrate a short distance into the convective anvil. The *Cloudsat* radar is able to penetrate through the anvil, revealing various structural elements including some cumulus congestus forming beneath the anvil. *CALIPSO* also reveals boundary layer clouds on both side of the convective region. On the left side, the boundary layer cloud tops are sloping upward toward the region of active convection. *Cloudsat* is able to detect some of the boundary layer cloud—mostly the cloud nearer the convective region—but much of this cloud goes undetected because of the cloud's low radar reflectivity and the presence of surface clutter in the *Cloudsat* observations.

The cloud mask difference plot (Fig. 9e) shows a line of blue and orange-red around much of the anvil, indicating both false and failed detections around this boundary. Some of these apparent detection errors may well be a result of the temporal and spatial mismatch between the radar and lidar observations. However, some of the false detections may also be due to the finite rise time (shape) of the radar pulse and oversampling. In much the same way as the surface return spreads into the radar bins two to four bins above the surface (see Fig. 7) strong reflectivity boundaries can be expected to generate a similar effect, albeit a factor of 1000+ weaker.

Cloudsat frequently obtains elegant cross sections through frontal cloud systems, as shown in Fig. 10. This example highlights the complementary nature of the *CALIPSO* lidar and *Cloudsat* radar observations. As is often the case, the lidar shows a region of thin cloud that is not sufficiently reflective (at microwave frequencies) for *Cloudsat* to detect. The fact that *Cloudsat* cannot detect this cloud is useful information that places upper bounds on the water content and effective particle size that this cloud may have. Throughout much of the upper portion of the cloud, both radar and lidar obtain good-quality measurements that can be used in a combined radar–lidar retrieval technique (Donovan 2003). In optically thicker portions of the cloud system, the radar continues to provide insight into the vertical structure of the cloud well after the lidar is attenuated.

The difference mask (Fig. 10e) shows a number of blue regions, indicating bins where the lidar was not attenuated (according to the feature mask) but failed to detect clouds that are easily detected by the radar. One of the difficulties observed with the *provisional CALIPSO* vertical feature mask is a tendency in some instances to fail to identify bins where the lidar has been fully (or nearly fully) attenuated. To reduce bias in our false detection estimates (Table 1) that would be caused by unidentified regions of lidar attenuation, we added an additional threshold on the total 532-nm

backscatter signal beyond that used by the *CALIPSO* project operational code.

4. Summary and discussion

The purpose of the operational *Cloudsat* hydrometeor detection algorithm is to produce a cloud mask that identifies when the measured radar return power is likely to be due to clouds or other hydrometeors and when it is likely to contain only noise. The *Cloudsat* operational cloud mask is stored in the *Cloudsat* 2B-GeoProf data product and contains values between 0 and 40. Values greater than 5 indicate the location of likely hydrometeors, with increasing values indicating a reduced probability of false detection, as summarized in Table 1.

Several examples of the *Cloudsat* cloud mask were given in section 3. These examples highlight both strengths and weaknesses of the *Cloudsat* data, as well as highlight the complementary nature of the *CALIPSO* lidar and *Cloudsat* radar observations.

The *Cloudsat* cloud mask is performing largely as anticipated prior to satellite launch. The percent of false detections (as estimated by comparison with *CALIPSO* lidar observations) for weak detections (cloud mask levels up to 20) is meeting expectations. For strong detections (cloud mask levels 30 and 40) the false detection rates are low, but not quite as low as expected. Examination of difference masks, such as those shown in Figs. 8, 9, and 10, indicates a mixture of false and failed detections around the boundaries of clouds, especially where there is a sharp cloud edge, such as near the anvil cloud in Fig. 9. Some of these apparent detection errors are likely the result of the temporal and spatial mismatch between the radar and lidar observations and the difference in bin resolution between the two instruments. Consequently, the estimated false and failed detection rates are likely to be overestimates.

While the purpose of this paper was not to evaluate the *CALIPSO* vertical feature mask, we can comment on some aspects of these data. Overall, the feature mask worked well for our purposes. The most significant difficulty we encountered in this research was the tendency for the feature mask to sometimes flag cloud as aerosol (and vice versa) and to not flag some areas where the lidar was fully, or nearly fully, attenuated. Both of these difficulties can clearly be improved through construction of a joint radar–lidar cloud mask.

Overall, the most significant difficulty with the *Cloudsat* data is that surface clutter effectively reduces the radar sensitivity near the surface. Algorithms to improve hydrometeor detection within the surface clutter are under investigation, but the ability to detect hydrometeors below 1.2 km is likely to remain reduced from that above 1.2 km.

Given its limited sensitivity and resolution and surface clutter difficulties, *Cloudsat* is unable to detect much of the thin cloud identified by the *CALIPSO* lidar. For the preliminary test set examined here, the percentage of failed detections—given as the number of failed detection divided by the total successful detections—exceeded 35%. Ultimately, we plan to use retrievals of cloud particle size and condensate from *Cloudsat* and *CALIPSO* in combination with other A-Train sensors to characterize the microphysics of those clouds that are detected by *Cloudsat* and those that are not. Nonetheless, it is critical when using *Cloudsat* data in model evaluations and science studies to carefully consider the effect of *Cloudsat* resolution and detection capabilities.

Acknowledgments. The authors would like to express their thanks to Phil Partain, Don Reinke, and the entire staff of the CloudSat Data Processing Center at CIRA/Colorado State University for gathering, processing, and providing CloudSat data, as well as to Chip Trepte and the *CALIPSO* team. This research was supported by the NASA CloudSat mission under the guidance of Debora Vane at the NASA Jet Propulsion Laboratory.

REFERENCES

Clothiaux, E. E., M. A. Miller, B. A. Albrecht, T. P. Ackerman, J. Verlinde, D. M. Babb, R. M. Peters, and W. J. Syrett, 1995: An evaluation of a 94-GHz radar for remote sensing of cloud properties. *J. Atmos. Oceanic Technol.,* **12,** 201–229.

——, T. P. Ackerman, G. G. Mace, K. Moran, R. T. Marchand, M. A. Miller, and B. E. Martner, 2000: Objective determination of cloud heights and radar reflectivities using a combination of active remote sensors at the ARM CART sites. *J. Appl. Meteor.,* **39,** 645–665.

Donovan, D. P., 2003: Ice-cloud effective particle size parameterization based on combined lidar, radar reflectivity, and mean Doppler velocity measurements. *J. Geophys. Res.,* **108,** 4573, doi:10.1029/2003JD003469.

Mace, G. G., R. Marchand, Q. Zhang, and G. Stephens, 2007: Global hydrometeor occurrence as observed by CloudSat; initial observations from summer 2006. *Geophys. Res. Lett.,* **34,** L09808, doi:10.1029/2006GL029017.

Stephens, G. L., and Coauthors, 2002: The Cloudsat Mission and the A-Train. *Bull. Amer. Meteor. Soc.,* **83,** 1771–1790.

Vaughan, M., S. Young, D. Winker, K. Powell, A. Omar, Z. Liu, Y. Hu, and C. Hostetler, 2004: Fully automated analysis of space-based lidar data: An overview of the *CALIPSO* retrieval algorithms and data products. *Laser Radar Techniques for Atmospheric Sensing,* U. N. Singh, Ed., International Society for Optical Engineering (SPIE Proceedings, Vol. 5575), 16–30.